Materials Horizons

Accepted Manuscript

Published on 17 October 2026
Licence and permissions

Check for updates



This is an Accepted Manuscript, which has been through the Royal Society of Chemistry peer review process and has been accepted for publication.

Accepted Manuscripts are published online shortly after acceptance, before technical editing, formatting and proof reading. Using this free service, authors can make their results available to the community, in citable form, before we publish the edited article. We will replace this Accepted Manuscript with the edited and formatted Advance Article as soon as it is available.

You can find more information about Accepted Manuscripts in the Information for Authors.

Please note that technical editing may introduce minor changes to the text and/or graphics, which may alter content. The journal's standard Terms & Conditions and the Ethical guidelines still apply. In no event shall the Royal Society of Chemistry be held responsible for any errors or omissions in this Accepted Manuscript or any consequences arising from the use of any information it contains.

ROYAL SOCIETY OF CHEMISTRY

rsc.li/materials-horizons

New concepts

Zero thermal expansion (ZTE) Materials plays a vital role in high-precision instruments and devices owing to their size stability under thermal shocks. However, conventional ZTE materials usually suffer from narrow working windows limited below 500 K, severely restricting their high-temperature practical applications in precision optics and aerospace devices. Differing from conventional structural regulation strategies for thermal expansion modulation, we propose a ferroelectric-active multi-ion synergy strategy to achieve broad-temperature ZTE behavior in traditional $PbTiO_3$-based perovskite ferroelectrics. The synergistic electron density reorganization of polar Bi^{3+}, Cu^{2+}, and W^{6+} ions enhances ferroelectric distortion, while Cu-induced van Hove singularities near the Fermi level dominate elastic lattice anomalies and enable robust wide-temperature ZTE. This work clarifies the intrinsic electronic mechanism of high-temperature ZTE, breaks the low-temperature bottleneck of traditional ZTE materials, and provides a universal ion-doping paradigm for designing high-temperature thermal-stable functional ceramics.

Materials Horizons Accepted Manuscript

Engineering Zero Thermal Expansion over a Wide Temperature Range in $PbTiO_3$-Based Ferroelectrics

Zhao Pan[1,*], Mengqi Ye[1,3], Yan Suo[2], Duo Wang[2,*], Xi Shen[1], Maocai Pi[1,3], Guangkai Zhang[1], Xubin Ye[1], Yao Shen[1], Richeng Yu[1], and Youwen Long[1,*]

[1]*Beijing National Laboratory for Condensed Matter Physics, Institute of Physics, Chinese Academy of Sciences, Beijing 100190, China*

[2]*Faculty of Applied Sciences, Macao Polytechnic University, Macao, SAR 999078, China*

[3]*University of Chinese Academy of Sciences, Beijing 100049, China*

Corresponding author: zhaopan@iphy.ac.cn; duo.wang@mpu.edu.mo; ywlong@iphy.ac.cn

Materials Horizons Accepted Manuscript

New concept

Zero thermal expansion (ZTE) Materials plays a vital role in high-precision instruments and devices owing to their size stability under thermal shocks. However, conventional ZTE materials usually suffer from narrow working windows limited below 500 K, severely restricting their high-temperature practical applications in precision optics and aerospace devices. Differing from conventional structural regulation strategies for thermal expansion modulation, we propose a ferroelectric-active multi-ion synergy strategy to achieve broad-temperature ZTE behavior in traditional $PbTiO_3$-based perovskite ferroelectrics. The synergistic electron density reorganization of polar Bi^{3+}, Cu^{2+}, and W^{6+} ions enhances ferroelectric distortion, while Cu-induced van Hove singularities near the Fermi level dominate elastic lattice anomalies and enable robust wide-temperature ZTE. This work clarifies the intrinsic electronic mechanism of high-temperature ZTE, breaks the low-temperature bottleneck of traditional ZTE materials, and provides a universal ion-doping paradigm for designing high-temperature thermal-stable functional ceramics.

Materials Horizons Accepted Manuscript

Abstract

Thermal expansion mismatches in precision optics, aerospace, and electronics can lead to delamination and fatigue, driving urgent demand for zero thermal expansion (ZTE) materials. At present, the majority of single-phase ZTE materials only function effectively below 500 K, limiting potential applications in many critical fields. Herein, we employ high-pressure and high-temperature synthesis to develop $(1-x)PbTiO_3$–$xBi(Cu_{3/4}W_{1/4})O_3$ perovskite ferroelectrics, utilizing spontaneous volume ferroelectrostriction to achieve an ultrawide ZTE regime from 300 to 725 K. In situ synchrotron X-ray diffraction tracks the lattice contraction and phase stability, while transmission electron microscope provides insights into atomic-scale A/B-site cation displacements and tetragonal distortions. First-principles calculations reveal that polar ferroelectric-active Bi^{3+}, Cu^{2+}, and W^{6+} ions synergistically reorganize electron density to reinforce ferroelectric distortion, while Cu-derived van Hove singularities near the Fermi level dominate the density of states and govern the elastic anomalies linked to the ultrawide ZTE behaviors. This study extends the scope of high-temperature ZTE materials and establishes a ferroelectric-active ion-doping strategy to engineer thermal expansion.

Materials Horizons Accepted Manuscript

1. Introduction

Thermal expansion is an intrinsic property of virtually all condensed matter; however, the positive coefficient of thermal expansion (CTE) that characterizes most materials poses a fundamental constraint on the reliability and longevity of advanced technological systems.[1,2] In multi-material devices, differential thermal expansion among dissimilar components can induce mechanical stress, leading to interfacial delamination and microcracking, ultimately resulting in catastrophic failure during thermal cycling. Such degradation is detrimental to precision optical systems, aerospace instrumentation, semiconductor packaging, and high-temperature electromechanical devices, where dimensional stability over a broad operational window is essential. Consequently, the development of materials exhibiting zero thermal expansion (ZTE) — defined by negligible dimensional changes upon heating or cooling with the absolute value of the average volumetric CTE of $\bar{\alpha}_V$ less than 2.0 $\times$ 10^{-6}/K — has become a central strategic objective in modern materials research.[3,4] However, ZTE compounds are rare, exemplified by Invar alloys,[5] $Fe[Co(CN)_6]$,[6] and nano $Mn_3Cu_{1-x}Ge_xN$,[7] and most reported ZTE materials are restricted to relatively low temperatures and narrow temperature ranges below 500 K. To realize ZTE, the prevailing and most versatile strategy is the rational design of engineered composites containing at least one negative thermal expansion (NTE) phase. NTE materials, which contract upon heating and expand upon cooling within specific temperature ranges, serve as the core technological enabler for CTE management, allowing for precise tailoring of the net thermal expansion of a composite to achieve positive, negative, or near-zero values.[8] Over the past several decades, a broad spectrum of NTE compounds has been examined, including framework oxides such as the ZrW_2O_8 family[9] and β-$LiAlSiO_4$,[10] metallic alloys (e.g., Invar Fe-Ni alloys),[11-14] cyanide frameworks (e.g., $Cd(CN)_2$),[15,16] nano materials such as CuO nanoparticles,[17] metal fluorides (e.g., ScF_3),[18-20] two-dimensional materials,[21,22] reduced layered ruthenates (e.g., $CaRuO_4$),[23,24] and perovskite/antiperovskite ceramics (e.g., $PbTiO_3$ (PT), $BiNiO_3$, and $Mn_3Cu_{1-x}Ga_xN$).[25-28] Despite this expanding materials portfolio, only a small fraction of these NTE candidates have proven effective as high-performance

Materials Horizons Accepted Manuscript

thermal expansion compensators, primarily owing to insufficient NTE magnitudes and/or narrow operational temperature windows.[3,29] Therefore, achieving ZTE over a wide, technologically relevant temperature range remains a significant scientific and engineering challenge.

PT is a typical perovskite-type (ABO_3) ferroelectric that shows unique NTE behavior from room temperature (RT) up to its Curie temperature (T_C = 763 K), with $\bar{\alpha}_V = -1.99 \times 10^{-5}$/K.[30] Numerous PT-based compounds have been reported to exhibit NTE from RT to their T_C.[3,31-34] The structural flexibility of the PT perovskite framework enables its NTE to be widely tuned through chemical modification, from $\bar{\alpha}_V = -0.11 \times 10^{-5}$/K to -3.92 $\times 10^{-5}$/K. However, achieving low or near-ZTE behavior often necessitates a reduction of the operating temperature range, that is, reducing the T_C, as observed in $Pb_{0.8}La_{0.2}TiO_3$ ($\bar{\alpha}_V = -0.11 \times 10^{-5}$/K, 300 - 400 K). The challenge remains to extend the ZTE into higher temperature ranges. Because the volume shrinkage of PT-based perovskites occurs primarily along the polar *c*-axis of the tetragonal ferroelectric phase,[35] the *c*/*a* ratio is significantly associated with their T_C. Indeed, NTE over a wide temperature range has been observed in PT-based ferroelectrics with enhanced *c*/*a*, such as 0.95PT-0.05$BiGaO_3$ (*c*/*a* = 1.071, $\bar{\alpha}_V = -2.23 \times 10^{-5}$/K, 300–773 K) and 0.95PT-0.05$BiYbO_3$ (*c*/*a* = 1.066, $\bar{\alpha}_V = -2.18 \times 10^{-5}$/K, 300–820 K).[36,37] Conversely, compounds with low *c*/*a* ratios, such as $PbTi_{0.95}Fe_{0.05}O_3$ (*c*/*a* = 1.056, $\bar{\alpha}_V = -1.49 \times 10^{-5}$/K, 300 – 748 K) and $Pb_{0.85}Sr_{0.15}TiO_3$ (*c*/*a* = 1.047, $\bar{\alpha}_V = -1.11 \times 10^{-5}$/K, 300–673 K),[38,39] show NTE over a narrower temperature range compared with pristine PT. These results reveal that regulating the *c*/*a* ratio via chemical tuning controls the NTE/ZTE temperature range of PT-based tetragonal ferroelectric perovskites.

Moreover, the morphotropic phase boundary (*x* = 0.64) of the (1-*x*)PT-*x*$BiScO_3$ system exhibits remarkable piezoelectric properties, such as a high piezoelectric constant and elevated T_C,[40] which has increased the interest in general PT-Bi*Me*O_3 systems. Here, *Me* can refer to a single cation with a +3 valence or a mixture of cations with an average +3 valence. Bi^{3+} possessing a $6s^2$ stereochemically active

Materials Horizons Accepted Manuscript

lone-pair electron configuration analogous to that of Pb^{2+}, exhibits stronger hybridization with oxygen than Pb^{2+}, resulting in increased tetragonality, greater polarization, and higher T_C.[41] Therefore, enhanced Bi/Pb displacements accompanied by large *c*/*a* ratios are expected in (1-*x*)PT-*x*Bi*Me*O_3 solid solutions. Notably, B-site cations should possess strong polarity in these solutions to attain high T_C values. Our recent studies have shown that Cu^{2+} acts as a ferroelectric-active cation, and high-T_C (510 °C) PT-based ferroelectric thin films can be achieved by Cu^{2+} substitution.[42] However, there remains limited exploration into the impact of Cu^{2+} on the thermal expansion properties of PT. Herein, we designed and synthesized a novel (1-*x*)PT-*x*Bi*Me*O_3 system, specifically (1-*x*)PT-*x*Bi$(Cu_{3/4}W_{1/4})O_3$,[43] employing a high-pressure and high-temperature (HPHT) method; in this system, W^{6+}, another ferroelectric-active cation, was introduced for charge balance. Ultralow CTEs or ZTE were achieved over a wide temperature window from RT to near 800 K in the present (1-*x*)PT-*x*Bi$(Cu_{3/4}W_{1/4})O_3$ (hereafter denoted as (1-*x*)PT-*x*BCW) system. Using first principle simulations, two distinct mechanisms are revealed. In the real space, the enhanced asymmetry electric distribution gives rise to stronger polarity, which manifests macroscopically spontaneous volume ferroelectrostriction (SVFS, correlated with the *c*/*a* ratio). In reciprocal space, Cu-induced van Hove singularities near the Fermi level govern the thermodynamic properties and, in turn, the anomalous thermal expansion behavior.

2. Results and discussion

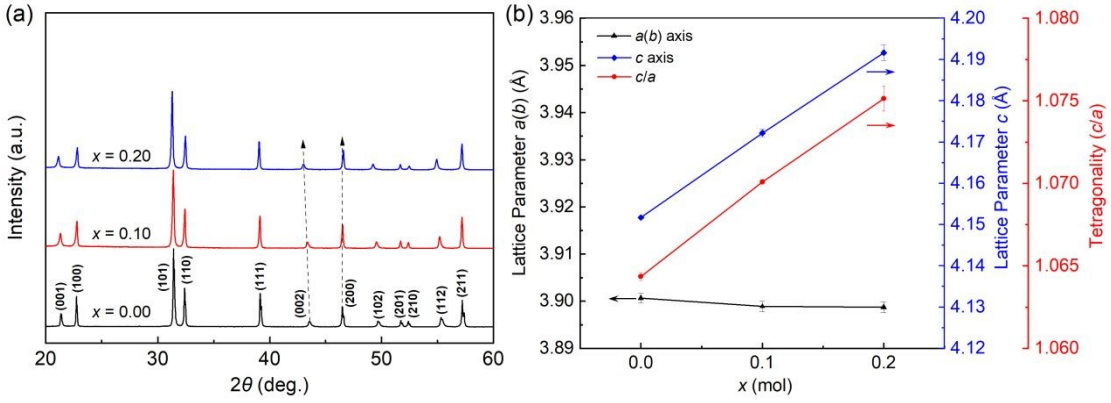


Figure 1. a) XRD patterns and b) lattice parameters of (1-*x*)PT-*x*BCW (x = 0.0 ~ 0.20) measured at room temperature.

Materials Horizons Accepted Manuscript

Figure 1(a) demonstrates the structural evolution of (1-*x*)PT-*x*BCW (*x* = 0, 0.10, and 0.20). All samples are of high purity, with no detectable impurities. 0.90PT-0.10BCW and 0.80PT-0.20BCW exhibit tetragonal perovskite structures similar to that of pristine PT. Impurity appears when *x* exceeds 0.20 (Fig. S1), indicating a solid solubility limit under the present synthesis conditions. As *x* increases, the (002) peak shifts towards lower angles, indicating a notable expansion of the *c*-axis. By contrast, the (200) peak shifts slightly towards higher angles, suggesting *a*-axis contraction. Consequently, the *c*/*a* ratio increases from 1.064 for pristine PT to 1.070 and 1.074 for 0.90PT-0.10BCW and 0.80PT-0.20BCW, respectively (Fig. 1(b)). To accurately determine the crystal structures of the prepared compounds, we performed SXRD experiments on 0.90PT-0.10BCW and 0.80PT-0.20BCW (Figs. S2 – S3). The detailed crystal structures were refined using the full-profile Rietveld method implemented in FullProf software.[44] The refined structural parameters are provided in the Supplemental Material (Table S1). The structures of 0.90PT-0.10BCW and 0.80PT-0.20BCW fit well when using the same initial model (space group *P*4*mm*, No. 99) used for PT. To investigate the structural characteristics of the prepared materials, we obtained spherical aberration-corrected HAADF Z-contrast STEM images (Fig. 2). Figures 2(a) and 2(d) clearly show the long-range ordered arrangements of A- and B-site cations, respectively; confirming the excellent crystalline quality. The average interplanar spacings of PT and 0.80PT-0.20BCW were measured by extracting intensity profiles along the *a*-axis (Figs. 2(b) and 2(e)) and *c*-axis (Figs. 2(c) and 2(f)) from randomly selected areas highlighted by orange and light-yellow lines, respectively. We then used the average values of the *a* and *c* parameters for lattice distortion analysis, yielding *c*/*a* ratios of 1.066 and 1.075 for PTO and 0.80PT-0.20BCW, respectively. These results agree well with those from SXRD refinement at RT.

Materials Horizons Accepted Manuscript

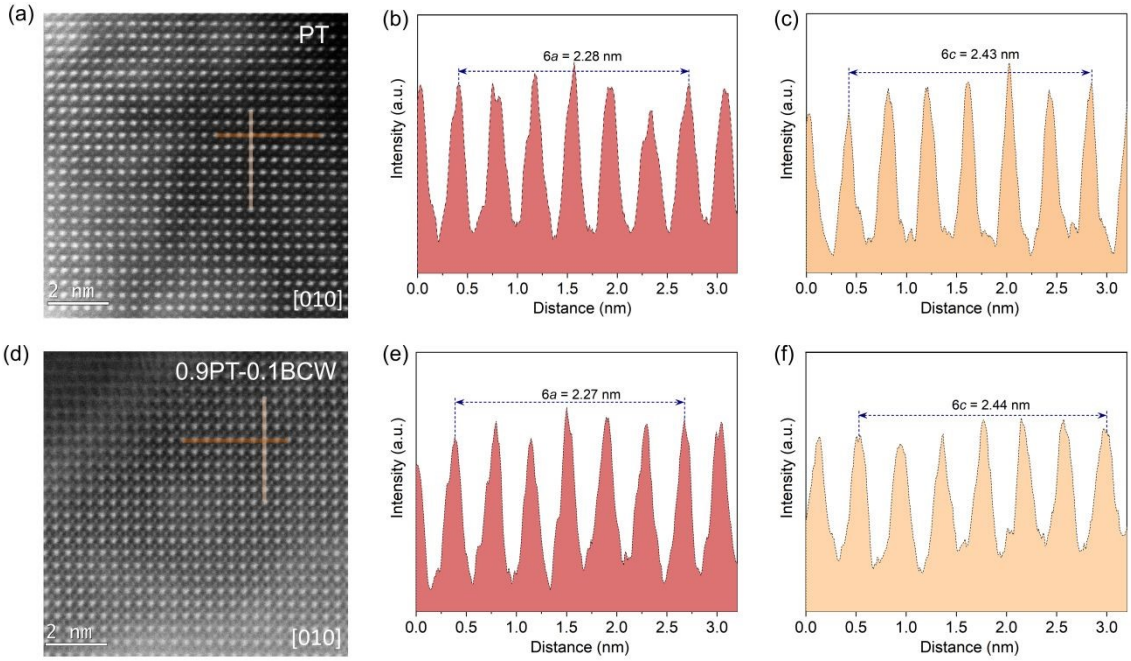


Figure 2. Atomic-scale HAADF-STEM images of a) PT and d) 0.80PT-0.20BCW compounds, six sets of interplanar spacing along b, e) *a* axis and c, f) *c* axis measured directly.

As mentioned earlier, NTE in PT-based ferroelectrics usually occurs from RT up to their T_C. In these materials, an enhanced *c*/*a* ratio is associated with an increased T_C.[3,45] Therefore, NTE over an extended temperature range can be achieved in PT-based ferroelectrics exhibiting enhanced *c*/*a* ratios. Temperature-dependent SXRD experiments were performed to study the thermal expansion properties of 0.90PT-0.10BCW and 0.80PT-0.20BCW, which exhibit higher *c*/*a* ratios than pure PT. The temperature dependence of the lattice parameters of these compounds was determined via Rietveld refinement of the SXRD data (Figs. 3(a) and 3(b)). As the temperature increases, the *c*-axis contracts rapidly, whereas the *a*(*b*)-axis slightly expands for 0.90PT-0.10BCW and 0.80PT-0.20BCW. Consequently, 0.90PT-0.10BCW demonstrates NTE over a wider temperature range than pristine PT ($\overline{\alpha}_V = -1.99 \times 10^{-5}$/K, 300 – 763 K); specifically, its NTE occurs from RT to as high as 810 K, with $\overline{\alpha}_V = -1.90 \times 10^{-5}$/K. Notably, over the temperature range from RT to 650 K, the unit cell volume of the compound shows minimal temperature dependence, exhibiting near-ZTE with an ultralow CTE of -0.82×10^{-6}/K (Fig. 3(c)). Similarly, as *x* increases, 0.8PT-0.2BCW demonstrates NTE across a wide temperature range

Materials Horizons Accepted Manuscript

from

RT to an elevated T_C of 830 K, with $\bar{\alpha}_V = -1.40 \times 10^{-5}$/K. More intriguingly, ZTE is achieved with a negligible CTE of -0.46×10^{-6}/K over an extended temperature range from RT to 725 K (Fig. 3(d)). The thermal expansion properties for representative ZTE materials are summarized in Table S2. Most ZTE compounds exhibit ZTE over narrow temperature ranges and at low temperatures, as exemplified by Invar alloys ($\bar{\alpha}_V = -0.46 \times 10^{-6}$/K, 278–303 K),[5] $Fe[Co(CN)_6]$ ($\bar{\alpha}_V = -4.41 \times 10^{-6}$/K, 4.2–300 K),[6] $Mn_3Cu_{0.5}Ga_{0.5}N$ ($\bar{\alpha}_V = 0.354 \times 10^{-6}$/K, 12–230 K),[7] and $N(CH_3)CuZn(CH_3)_4$ ($\bar{\alpha}_V = -0.6 \times 10^{-6}$/K, 200–400 K),[46] except for $Zr_{0.4}Sn_{0.6}Mo_2O_8$ ($\bar{\alpha}_V = -0.18 \times 10^{-6}$/K, 12 – 600 K)[47] and ScF_3 ($\bar{\alpha}_V = -0.702 \times 10^{-6}$/K, 300 – 900 K).[48] The ZTE observed in the present (1-*x*)PT-*x*BCW system extends to high temperatures, indicating its potential for future applications. The increased T_Cs and extended NTE/ZTE temperature ranges of these compounds coincide with their enhanced *c*/*a* ratios.

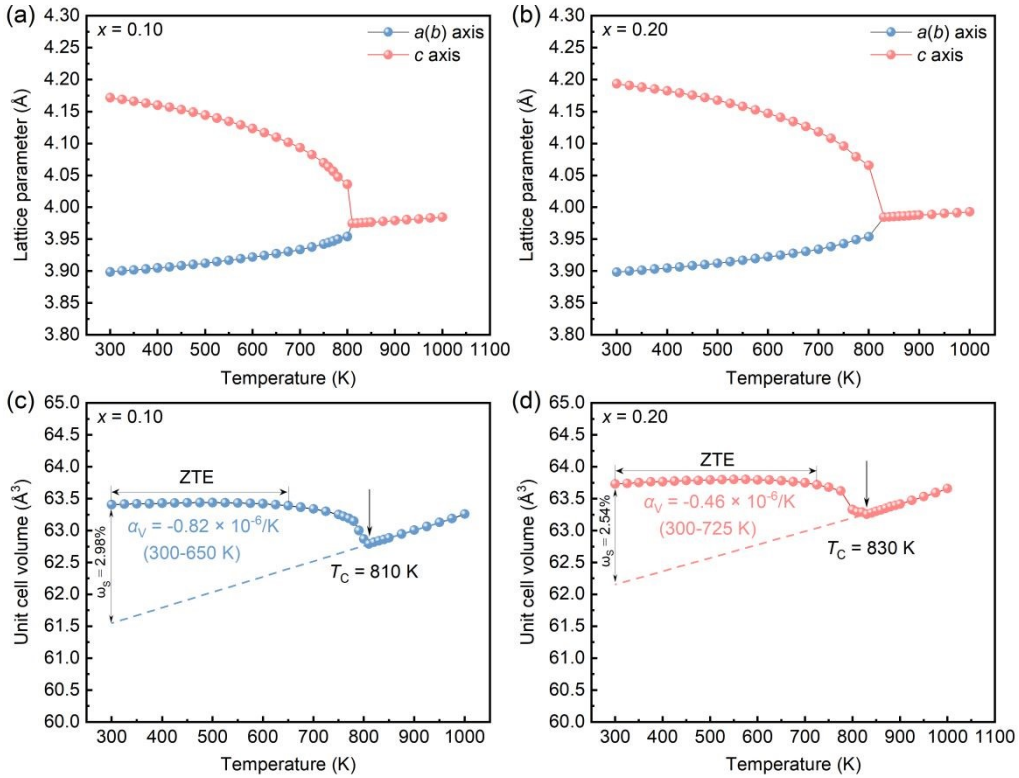


Figure 3. Lattice parameters of *a*(*b*) and *c* for a) *x* = 0.10 and b) *x* = 0.20, and the corresponding unit cell volume as a function of temperature for c) *x* = 0.10 and d) *x* = 0.20 of the (1-*x*)PT-*x*BCW compounds. An illustration of spontaneous volume ferroelectrostriction (ω_S) is also provided. The

Materials Horizons Accepted Manuscript

T_C values are 810 K and 830 K for the x = 0.10 and x = 0.20 compounds, respectively.

We now discuss the mechanism underlying the unique NTE/ZTE occurring within the same material. Theoretical and experimental studies indicate that ferroelectric behavior significantly influences the NTE properties of PT-based ferroelectrics.[3,31,49] SVFS (ω_S) was used to quantify the effect of ferroelectricity on volume changes observed in the ferroelectric phase of PT-based materials.[50] SVFS provides a baseline by accounting for thermal expansion solely owing to phonon vibrations, defined as follows:

$$\omega_S = \frac{V_{exp} - V_{nm}}{V_{nm}} \times 100\% \qquad (1)$$

where V_{exp} denotes the experimental unit cell volume and V_{nm} signifies the nominal unit cell volume, estimated by extrapolating from the paraelectric to the ferroelectric phase. A high ω_S value indicates a strong ferroelectrovolume effect and increased NTE, whereas a low value indicates weak NTE. The ω_S values for 0.90PT-0.10BCW and 0.80PT-0.20BCW are 2.98% and 2.54%, respectively (Fig. 3), both lower than that of pristine PT (ω_S = 3.1%). This weakening of the SVFS effect accounts for the decrease in NTE and the appearance of ZTE observed in the present (1-x)PT-xBCW system. Notably, the broad ZTE plateau is governed not only by the total magnitude of SVFS, but more critically by its temperature distribution. In pristine PT, major volume contraction concentrates within ~100 K below T_C,[51,52] while $Bi(Cu_{3/4}W_{1/4})O_3$ doping spreads this contraction over a much wider temperature range. Such redistribution is mainly controlled by compositional disorder from mixed A- and B-site cations, which produces a distribution of local T_Cs and smears the sharp first-order phase transition of pure PT. Meanwhile, enhanced global/local tetragonality elevates macroscopic T_C and expands the ferroelectric stability window. In short, the suppressed SVFS controls the compensation magnitude, and temperature redistribution of ferroelectrostriction determines the ZTE temperature window, with the two effects operating synergistically.

In perovskite ferroelectrics, the hybridization of A/B-site cations with oxygen is

Materials Horizons Accepted Manuscript

essential for polar distortion.[53-55] To investigate the mechanisms underlying electric polarization and NTE in the (1-*x*)PT-*x*BCW compounds, we performed *ab* initio density functional theory (DFT) simulations. According to modern polarization theory,[56] polarization originates from off-center ionic displacement and asymmetrical electron distribution. Because spontaneous polarization in PT-based materials primarily occurs along the *c* direction, our analysis focuses on polarization along this crystallographic direction. We first analyze the ionic displacement to directly study its ionic contribution. Subsequently, we examine the electronic contribution by analyzing the real-space charge distribution using charge density and electron localization function (ELF) data, together with the reciprocal-space electronic properties characterized by the spectral function, band structure, and density of states (DOS), emphasizing the role of DOS peaks and Van Hove singularities near the Fermi level.

BCW substitution significantly increases displacements at A and B sites, as shown in Table S3. At the A site, the displacements for the doped Bi and Pb atoms are −0.19 and −0.10 Å, respectively, compared with −0.09 Å for pure PT. At the B site, the displacements for Cu, W, and Ti atoms are 0.16, 0.33, and 0.19 Å, respectively, compared with 0.12 Å for pure PT. By contrast, the ligand O atoms show only a slight change of approximately 0.50 Å, which is close to the 0.44 Å displacement observed for the pristine compound. This finding suggests that the ionic contribution to electric polarization from cation sites increases after BCW substitution. Additionally, we analyzed changes in the *c/a* ratio within the local AO_{12} and BO_6 environments induced by A- and B-site substitutions. As summarized in Table S4, the average local *c/a* ratios for the Bi-, Cu-, and W-substituted structures are 1.08, 1.18, and 1.04, respectively, compared with 1.06 for pristine PT. Bi substitution and the associated moderate enhancement of *c/a* ratio suggest stronger local tetragonal distortion.

The contribution of electronic asymmetry can be qualitatively illustrated by the charge density and ELF distribution shown in Fig. S3. For the A site, the overall electron population increases post-substitution relative to pure PT, as evidenced by the denser contours between Pb/Bi and O in the upper panel of Fig. S4(a). This enhancement is more pronounced around the Bi atom, where electrons are more

Materials Horizons Accepted Manuscript

localized along the −*c* direction, leading to a relatively stronger electronic asymmetry along this axis. At the B site, Cu and W substitution introduce additional valence electrons into the system and, more importantly, induce a polarized electronic population along the *c* direction, as illustrated by the pronounced localized states around the substituted Cu and W atoms. This effect is particularly apparent in the additional contour shown in the lower right panel of Fig. S4(b). Cu shows a slightly greater and more localized electron accumulation than W, which can be attributed to the relatively larger displacement of Cu ions compared with the surrounding O atoms.

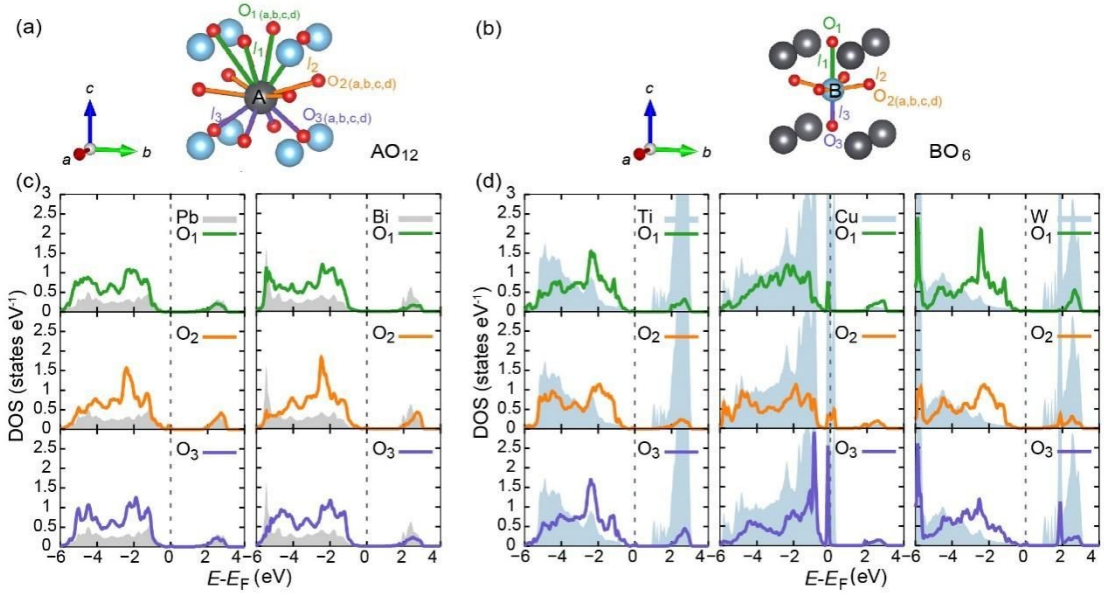


Figure 4. Representative local environments around a) A site (PbO_{12}) and b) B site (TiO_6) are displayed, with corresponding electronic density of states shown in c) and d), respectively. The Pb, Ti and O atom are represented by grey, cyan and red color, respectively. Different bond lengths are labeled as l_1, l_2 and l_3, highlighted in green, orange and purple, correspondingly.

The observed asymmetric electron distribution is well reflected in the electronic spectral function, where the cation-ligand hybridization pattern and its relative strength vary significantly. Such variations are governed by the local environment, which is characterized by the distinct bonding characteristics of the nearest-neighbor A/B–O pairs. Two types of local polyhedra, AO_{12} and BO_6, are shown in Figs. 4(a) and 4(b), respectively. Because of the substantial cation displacement along the *c* direction, the nearest A/B–O bonds are categorized into three groups, labeled l_1, l_2,

Materials Horizons Accepted Manuscript

and l_3, as shown in Table S5, corresponding to the longest, intermediate, and shortest bond lengths, respectively. The corresponding O-projected DOS is denoted using the same labeling scheme. Given that O_1 and O_3 occupy equivalent Wyckoff positions, both exhibit similar DOS shapes at the A (Fig. 4(c)) and B (Fig. 4(d)) sites. For instance, in the case of O within TiO_6 (left panel in Fig. 4(d)), the primary DOS peak appears at approximately −2 eV for O_1 and O_3. By contrast, the O_2 peak broadens and shifts slightly to higher energy, while the peak near −4 eV becomes more pronounced. A noteworthy feature can be observed in the Cu-related data. As shown in the middle panel of Fig. 4(d), Cu substitution introduces a characteristic peak at the Fermi level, leading to strong, orientation-dependent hybridization between Cu and neighboring O atoms. The hybridization of O_3, which is bonded to Cu along the $-c$ direction, is particularly strong, indicating a stronger Cu–O bond. The presence of a peak at the Fermi level often suggests unusual physical behavior. In the present case, it is associated with NTE, which can be attributed to a van Hove singularity in the electronic structure.[57]

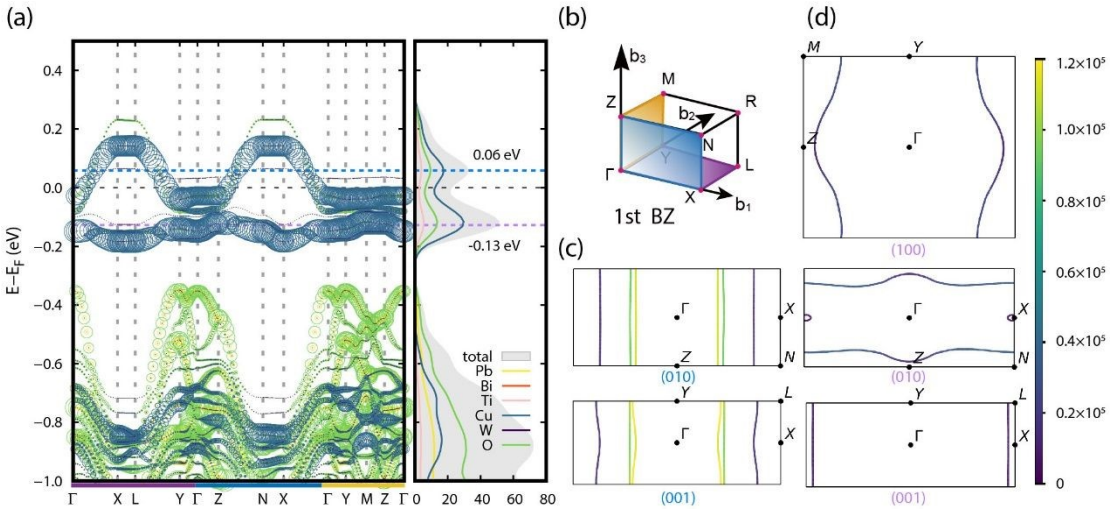


Figure 5. a) Atom-projected band structure and corresponding PDOS (projected Density of States) in PT-BCW. The black, blue, and purple dashed horizontal lines indicate the Fermi level and the energies corresponding to the two DOS peaks, respectively. b) Schematic diagram of the first Brillouin zone in PT-BCW. c, d) Constant-energy contours corresponding to the two total-DOS peaks.

The van Hove singularity corresponds to extrema or saddle points in the

Materials Horizons Accepted Manuscript

electronic band structure. Those located near the Fermi level are of particular importance because they can strongly influence the elastic response and, consequently, thermodynamic properties of the material. Because thermal expansion is related to the pressure derivatives of the elastic moduli, pronounced anomalies in thermal expansion are expected. The calculated band structure and projected DOS around the Fermi level are shown in Fig. 5(a). Several relatively flat bands, primarily originating from the substituted Cu atoms, appear within the energy window of −0.2 to 0.2 eV. Thus, two pronounced DOS peaks appear at 0.06 and −0.12 eV. It is worth noting that even if the spin polarization is considered, the critical branches contributing to two peaks at 0.06 and -0.13 remain unchanged as shown in Fig. S5. For the DOS peak above the Fermi level, the corresponding bands exhibit a nearly flat profile along two high-symmetry paths, N-X-L and Z-G-Y-M-Z, aligned with two parallel planes normal to the b_1 direction in reciprocal space, as illustrated in Fig. 5(b). At 0.06 eV, the resulting singularity is clearly manifested in the constant-energy contours projected onto the (010) and (001) planes. The corresponding Van Hove pockets appear as nearly parallel contour segments extending along the X-N and X-L directions, as shown in Fig. 5(c). By contrast, for the DOS peak below the Fermi level, the flat-band features remain nearly unchanged, except along the X-N direction, where an additional extremum emerges at point X. Consequently, as shown in Fig. 5(d), although the constant-energy contours in the (001) plane remain largely unchanged from those associated with the peak above the Fermi level, an additional pocket appears around X in the (010) plane . Because this energy intersects a flat band along the Z-G-Y-M-Z path, new pockets emerge along the Z-N and Z-M directions, as shown in the (010) and (100) planes. In particular, the latter pocket first appears at point M at −0.12 eV and gradually expands along the Z direction as energy decreases, eventually evolving into a van Hove pocket that encompasses points M and Z at −0.13 eV, as illustrated in Fig. S6.

We comprehensively analyzed the ionic displacements and charge distributions induced by A- and B-site substitution and elucidated the mechanisms underlying the enhanced electric polarization and local *c*/*a* ratio observed in these compounds using

Materials Horizons Accepted Manuscript

first-principles simulations. Further analysis of the electronic structure reveals the significant effects of Cu substitution, which gives rise to two characteristic DOS peaks associated with Van Hove singularities near the Fermi level. These unique characteristics are closely associated with low-energy electronic excitations and the corresponding elastic response, which are expected to contribute to the ZTE observed in the (1-*x*)PT-*x*BCW system.

3. Conclusion

In summary, we designed and prepared a new ferroelectric ZTE system, (1-*x*)PT-*x*BCW (*x* = 0.10 and 0.20), employing an HPHT method. Rietveld refinement of powder SXRD data, combined with TEM analysis, revealed enhanced *c*/*a* ratios in the present (1-*x*)PT-*x*BCW compounds relative to pristine PT. Intriguingly, these compounds demonstrated favorable ZTE with a negligible CTE of -0.46×10^{-6}/K over a wide temperature range from RT up to 725 K. This unique phenomenon arises from the introduction of A/B-site cations with strong polarity, such as Bi^{3+}, Cu^{2+}, and W^{6+}, which redistribute electronic density. Especially, according to first-principles calculations, Cu-derived van Hove singularities near the Fermi level dominate the density of states and govern the elastic anomalies linked to the ultrawide ZTE behaviors. The present study expands the scope of high-temperature ZTE materials in ferroelectric materials and establishes a ferroelectric-active ion-doping strategy for engineering thermal expansion.

4. Experimental Section

Materials Preparation. A cubic anvil-type high-pressure apparatus was used to prepare samples of the (1-*x*)$PbTiO_3$-*x*$Bi(Cu_{3/4}W_{1/4})O_3$ (*x* = 0.1 and 0.2, abbreviated as (1-*x*)PT-*x*BCW) compounds. The raw materials of high-purity PbO (99.9%, Thermo Scientific), TiO_2 (99.99%, Aladdin), Bi_2O_3 (99.99%, Innochem), CuO (99.9%, MACKLIN), and WO_3 (99.99%, MACKLIN) were throughly mixed according to the stoichiometry. The mixtures were then sealed in a gold capsule and was reacted at 6 GPa and 1373 K for 30 min. To remove mechanical strain introduced during the high pressure synthesis, the obtained samples were carefully ground and annealed at 400 ℃

Materials Horizons Accepted Manuscript

for an hour before cooling to room temperature.

Characterizations. A diffractometer (Huber, Germany) was used to collect the X-ray diffraction (XRD) patterns for phase identification. High-temperature synchrotron X-ray powder diffraction (SXRD) experiments were performed on the BL02B2 beamline of SPring-8 with a wavelength of 0.42 Å.[58] Using the *FullProf* software, the detailed crystal structure was refined based on the full-profile Rietveld method. The high-angle annular dark field (HAADF) investigations were performed on Cs-corrected transmission electron microscope (JEM-ARM200F, JEOL, Japan). Polarized Raman-scattering data were obtained using a MonoVista CRS+ 500 spectrometer (Spectroscopy & Imaging, Germany).

First-principles calculations. Based on experimental structure data with lattice parameters of $a = b = 3.90$ Å, $c = 4.17$ Å, a $2 \times 5 \times 4$ supercell with 200 atoms was constructed to model the 0.9PT-0.1BCW compound. For comparing the effect of doped atoms, a pristine PT model with experimental lattice parameters of $a = b = 3.90$ Å, $c = 4.15$ Å was also considered. The theoretical simulations were performed by first-principle method implemented in Vienna ab-initio Simulation Package (VASP).[59] The projector-augmented wave (PAW) pseudopotential and local density approximations (LDA) were employed to treat the electron-ion interactions and the exchange-correlation functional, respectively. A plane-wave energy cutoff of 600 eV was chosen for the basis set. The structure optimization was performed by relaxing the atomic positions while keeping the experimental lattice parameters fixed. The convergence thresholds for ionic and electronic iterations was set to -0.01 eV/atom and 1×10^{-7} eV. The k-point meshes used for structural optimization, static self-consistent calculation (including constant-energy surface analysis and ELF extraction), and DOS calculations were $5 \times 2 \times 2$, $8 \times 3 \times 4$, and $10 \times 4 \times 5$, respectively. The python library IFermi[60] was used to generate and visualize the 2D slices of the energy surface around Fermi energy in reciprocal space.

Author Contributions

Z. P. conceived the idea of the work. Z.P. fabricated the samples and performed the

Materials Horizons Accepted Manuscript

initial tests with the help from M.Y. Y.S. performed the theoretical calculations under the supervision of D.W. Z.P., M.P., and X.Y. performed the synchrotron X-ray diffraction experiments. X.S. and R.Y. performed and analyzed the STEM experiments. Z.P. wrote the original manuscript. All authors discussed the results and commented on the manuscript. Z.P., D.W., and Y.L. guided the projects.

Conflict of Interest

The author declare no competing interests.

Data Availability Statement

The data that support the findings of this study are available in the supplementary information (SI) of this article. The supplementary information includes part of the detailed electronic structure calculations, additional characterization data, and supporting figures and tables related to this study.

Acknowledgements

This work was supported by the National Natural Science Foundation of China (12425403, 22271309, and 12304268), the National Key R&D Program of China (Grant No. 2021YFA1400300 and 2025YFE0202100), the Beijing Natural Science Foundation (Grant No. F251005), and the Strategic Priority Research Program (B) of the Chinese Academy of Sciences (CAS) (No. XDB1720000). Duo Wang acknowledges financial support from the Science and Technology Development Fund from Macao SAR (Grant No. 0062/2023/ITP2, 0016/2025/RIA1) and the Macao Polytechnic University (Grant No. RP/FCA-03/2023, RP/FCA-20/2025). The synchrotron radiation experiments were performed at BL02B2 in SPring-8 with the approval of the Japan Synchrotron Radiation Research Institute (JASRI) (Proposal No. 2024B1807, 2025A1495, and 2025B1628).

References

1 K. Takenaka, *Sci. Technol. Adv. Mater.*, 2012, **13**, 013001.

2 Y. Q. Liu, N. K. Shi, C. Zhou and J. Chen, *Chem. Mater.*, 2026, **38**, 8741.

3 J. Chen, L. Hu, J. X. Deng and X. R. Xing, *Chem. Soc. Rev.*, 2015, **44**, 3522.

Materials Horizons Accepted Manuscript

4 M. T. Dove and H. Fang, *Rep. Prog. Phys.*, 2016, **79**, 066503.

5 A sleight, *Nature*, 2003, **425**, 674.

6 S. Margadonna, K. Prassides and A. N. Fitch, *J. Am. Chem. Soc.*, 2004, **126**, 15390.

7 X. Y. Song, Z. Sun, Q. Z. Huang, M. Rettenmayr, X. Liu, M. Seyring, G. Li, G. Rao and F. X. Yin, *Adv. Mater.*, 2011, **23**, 4690.

8 C. S. Coates and A. L. Goodwin, *Mater. Horiz.*, 2019, **6**, 211.

9 T. A. Mary, J. S. O. Evans, T. Vogt and A. W. Sleight, *Science*, 1996, **272**, 90.

10 A.W. Sleight, *Inorg. Chem.*, 1998, **37**, 2854.

11 M. V. Schilfgaarde, I. A. Abrikosov and B. Johansson, *Nature*, 1999, **400**, 46.

12 Z. Pan, H. Zhou, C. Chen, Y. Cao, X. Ye, R. Wang, S. Kawaguchi, X. Xing and Y. Long, *J. Am. Chem. Soc.*, 2026, **148**, 12119.

13 W. Yang, J. He, H. Zhou, C. Yu, Q. Zhang, J. Chen, K. Kato, C. Wang, W. Li, Y. Cao, Q. Li, L. You, F. Chen, K. Lin and X. Xing, *Adv. Funct. Mater.*, 2026, **36**, e22039.

14 Y. Li, T. Li, Y. Fu, D. J. Singh and L. Zhang, *J. Am. Chem. Soc.*, 2026, **148**, 38913.

15 A. L. Goodwin, M. Calleja, M. J. Conterio, M. T. Dove, J. S. O. Evans, D. A. Keen, L. Peters and M. G. Tucker, *Science*, 2008, **319**, 794.

16 Q. Gao, J. Wang, A. Sanson, Q. Sun, E. Liang, X. Xing and J. Chen, *J. Am. Chem. Soc.*, 2020, **142**, 6935.

17 X. G. Zheng, H. Kubozono, H. Yamada, K. Kato, Y. Ishiwata and C.N. Xu, *Nat. Nanotechnol.*, 2008, **3**, 724.

18 B. K. Greve, K. L. Martin, P. L. Lee, P. J. Chupas, K. W. Chapman and A. P. Wilkinson, *J. Am. Chem. Soc.*, 2010, **132**, 15496.

19 L. Hu, F. Qin, A. Sanson, L. Huang, Z. Pan, Q. Li, Q. Sun, L. Wang, F. Guo, U. Aydemir, Y. Ren, C. Sun, J. Deng, G. Aquilanti, J. M. Rondinelli, J. Chen and X. Xing, *J. Am. Chem. Soc.*, 2018, **140**, 4477.

20 D. Wendt, E. Bozin, J. Neuefeind, K. Page, W. Ku, L. Wang, B. Fultz, A. V. Tkachenko and I. A. Zaliznyak, *Sci. Adv.*, 2019, **5**, eaay2748.

21 L. X. Hou, X. P. Cui, B. Guan, S. Z. Wang, R. A. Li, Y. Q. Li, D. B. Zhu and J. Zheng, *Nature*, 2022, **606**, 507.

22 A. Shaikh, J. Q. Wu and B. Peng, *Phys. Rev. Lett.*, 2025, **135**, 126103.

Materials Horizons Accepted Manuscript

23 T. F. Qi, O. B. Korneta, S. Parkin, L. E. De Long, P. Schlottmann and G. Cao, *Phys. Rev. Lett.*, 2010, **105**, 177203.

24 K. Takenaka, Y. Okamato, T. Shinoda, N. Katayama and Y. Sakai, *Nat. Commun.*, 2017, **8**, 14102.

25 J. Chen, K. Nittala, J. S. Forrester, J. L. Jones, J. Deng, R. Yu and X. Xing, *J. Am. Chem. Soc.*, 2011, **133**, 11114.

26 M. Azuma, W. T. Chen, H. Seki, M. Czapski, S. Olga, K. Oka, M. Mizumaki, T. Watanuki, N. Ishimatsu, N. Kawamura, S. Ishiwata, M. G. Trucker, Y. Shimakawa and J. P. Attfield, *Nat. Commun.*, 2011, **2**, 347.

27 K. Takenaka and H. Takagi, *Appl. Phys. Lett.*, 2005, **87**, 261902.

28 Z. Pan, T. Nishikubo, H. Yamamoto, X. B. Ye, M. Azuma and Y. W. Long, *cMat*, 2025, **2**, e70017.

29 X. Jiang, N. Wang, L. Dong, M. S. Molokeev, S. Wang, Y. Liu, S. Guo, W. Li, R. Huang, S. Wu, L. Li and Z. Lin, *Mater. Horiz.*, 2022, **9**, 2207.

30 J. Chen, X. Xing, R. Yu and G. Liu, *J. Am. Ceram. Soc.*, 2005, **88**, 1356.

31 J. Chen, L. L. Fan, Y. Ren, Z. Pan, J. X. Deng, R. B. Yu and X. R. Xing, *Phys. Rev. Lett.*, 2013, **110**, 115901.

32 Z. Pan, J. Chen, R. Yu, L. Patra, P. Ravindran, A. Sanson, R. Milazzo, A. Carnera, L. Hu, L. Wang, H. Yamamoto, Y. Ren, Q. Huang, Y. Sakai, T. Nishikubo, T. Ogata, X. A. Fan, Y. Li, G. Li, H. Hojo, M. Azuma and X. Xing, *Chem. Mater.*, 2019, **31**, 1296.

33 T. Yang, K. Lin, Q. Li, Y. Wang, L. Gu, N. Wang, J. Deng, J. Chen and X. Xing, *Inorg. Chem. Front.*, 2020, **7**, 1284.

34 Z. Pan, Y. -W. Fang, S. A. Nikolaev, L. Wu, J. Zhang, M. Q. Ye, J. Liu, X. B. Ye, X. Wang, T. Nishikubo, Y. Sakai, R. Z. Yu, S. Kawaguchi, N. P. Lu, Y. Kuroiwa, J. Chen, M. Azuma, X. R. Xing and Y. W. Long, *Mater. Horiz.*, 2025, **12**, 6804.

35 H. Yamamoto, T. Imai, Y. Sakai and M. Azuma, *Angew. Chem. Int. Ed.*, 2018, **57**, 8170.

36 T. Yang, Y. Wang, L. Fan, N. Wang, K. Lin, J. Chen and X. R. Xing, *J. Phys. Chem. C*, 2020, **124**, 20445.

37 Z. Pan, F. Y. Zhou, M. Q. Ye, D. Wang, Q. M. Liu, T. Nishikubo, X. B. Ye, X. Wang, J. Liu, N. P. Lu, S. Kawaguchi, M. Azuma and Y. W. Long, *J. Adv.*

Materials Horizons Accepted Manuscript

Ceram., 2025, **14**, 9221096.

38 C. Sun, Z. M.Cao, J. Chen, R. B. Yu, X. Y. Sun, P. H. Hu, G. R. Liu and X. R. Xing, *Phys. Stat. Sol.* (*b*), 2008, **245**, 2520.

39 X. R. Xing, J. Chen, J. X. Deng and G. R. Liu, *J. Alloy. Compd.*, 2003, **360**, 286.

40 R. E. Eitel, C. A. Randall, T. R. Shrout and S. -E. Park, *Jpn. J. Appl. Phys.*, 2002, **41**, 2099.

41 M. Yashima, K. Omoto, J. Chen, H. Kato and X. R. Xing, *Chem. Mater.*, 2011, **23**, 3135.

42 W. Song, G. Xi, Z. Pan, J. Liu, X. Ye, Z. Liu, X. Wang, P. Shan, L. Zhang, N. Lu, L. Fan, X. Qin and Y. Long, *Chin. Phys. B*, 2024, **33**, 057701.

43 I. Grinberg and A. M. Rappe, *Phase Transit.*, 2007, **80**, 351.

44 J. Rodríguez-Carvajal, *CEA*/*Saclay*, *France* 2001, **1045**, 132.

45 Z. Pan, M. Q. Ye, Y. Suo, F. Y. Zhou, D. Wang, J. Liu, X. B. Ye, J. Zhang, M. C. Pi, W. H. Li, C. Chen, N. P. Lu, S. Kawaguchi, Y. Shen and Y. W. Long, *Rare Met.*, 2025, **44**, 6494.

46 A. E. Phillips, G. J. Halder, K. W. Chapman, A. L. Goodwin and C. J. Kepert, *J. Am. Chem. Soc.*, 2009, **132**, 10.

47 S. E. Tallentire, F. Child, I. Fall, L. Vella-Zarb, I. R. Evans, M. G. Tucker, D. A. Keen, C. Wilson and J. S. Evans, *J. Am. Chem. Soc.*, 2013, **135**, 12849.

48 L. Hu, J. Chen, L. L. Fan, Y. Ren, Y. C. Rong, Z. Pan, J. X. Deng, R. B. Yu and X. R. Xing, *J. Am. Chem. Soc.*, 2014, **136**, 13566.

49 F. Wang, Y. Xie, J. Chen, H. Fu and X. R. Xing, *Appl. Phys. Lett.*, 2013, **103**, 221901.

50 J. Chen, F. Wang, Q. Huang, L. Hu, X. Song, J. Deng, R. Yu and X. R. Xing, *Sci. Rep.*, 2013, **3**, 2458.

51 J. Chen, X. R. Xing, R. B. Yu and G. R. Liu, *J. Am. Ceram. Soc.*, 2005, **88**, 1356.

52 Z. Pan, Y. -W. Fang, T. Nishikubo, L. Hu, S. Kawaguchi and M. Azuma, *Chem. Mater.*, 2022, **34**, 2798.

53 R. E. Cohen, *Nature*, 1992, **358**, 136.

54 Y. Kuroiwa, S. Aoyagi, A. Sawada, J. Harada, E. Nishibori, M. Takata and M. Sakata, *Phys. Rev. Lett.*, 2001, **87**, 217601.

55 M. Yashima, K. Omoto, J. Chen, H. Kato and X. R. Xing, *Chem. Mater.*, 2011,

Materials Horizons Accepted Manuscript

23, 3135.

56 N. A. Spaldin, *J. Solid State. Chem.*, 2012, **195**, 2.

57 P. Souvatzis, O. Eriksson and M. I. Katsnelson, *Phys. Rev. Lett.*, 2007, **99**, 015901.

58 S. Kawaguchi, M. Takemoto, H. Tanaka, S. Hiraide, K. Sugimoto and Y. Kubota, *J. Synchrotron Radiat.*, 2020, **27**, 616.

59 G. Kresse and J. Furthmüller, *Phys. Rev. B*, 1996, **54**,11169.

60 A. M. Ganose, A. Searle, A. Jain and S. M. Griffin, *JOSS*., 2021, **6**, 3089.

Materials Horizons Accepted Manuscript

The data that support the findings of this study are available in the supplementary information (SI) of this article. The supplementary information includes part of the detailed electronic structure calculations, additional characterization data, and supporting figures and tables related to this study.

Materials Horizons Accepted Manuscript